Model-based FDI for Agile Spacecraft with Multiple Actuators Working Simultaneously

E. Lopez-Encarnacion [*], **R. Fonod** [*], **P. Bergner** [**]

[*] *Delft University of Technology, 2629 HS Delft, The Netherlands (e-mail: ericlopen@gmail.com, r.fonod@tudelft.nl)*
[**] *Airbus Defence and Space, 88090 Immenstaad am Bodensee, Germany (e-mail: patrick.bergner@airbus.com)*

Abstract: Fast and large-angle attitude slew maneuvers often imply simultaneous use of multiple actuators such as thrusters and reaction wheels (RWs). A fault in any of these actuators might lead to partial or full damage of sensitive spacecraft instruments. In this paper, a model-based Fault Detection and Isolation (FDI) strategy is proposed, which aims at detecting various actuator faults, such as stuck-open/closed thruster, thruster leakage, loss of effectiveness of all thrusters, and change of RW friction torque due to change of Coulomb and/or viscosity factor. The proposed FDI strategy is also able to detect and isolate faults affecting the RWs tachometer sensor. The FDI system design is based on a multiplicative extended Kalman filter and a generalized likelihood ratio thresholding of the residual signals. The performance and robustness of the proposed FDI strategy is evaluated using Monte Carlo simulations and carefully defined FDI performance indices. Preliminary results suggest promising performance in terms of detection/isolation times, miss-detection/isolation rates, and false alarm rates.

Keywords: Fault Detection and Isolation; Agile Spacecraft; Reaction Wheels; Thrusters.

1. INTRODUCTION

Spacecraft agility, meaning the capability of the spacecraft to change its attitude by performing fast attitude slew maneuvers or to follow a given attitude profile with high precision, is becoming more and more important for future space missions. These requirements demand the spacecraft to be equipped with actuators, such as thrusters and reaction wheels (RWs), capable of generating high reaction torques and perform attitude maneuvers with high angular rates. The control of the spacecraft attitude is achieved by the Attitude and Orbit Control System (AOCS), which includes sensors and actuators that are not exempt of faults. An incorrect AOCS fault management may cause severe degradation of the spacecraft performance and/or cause damage to sensitive spacecraft instruments.

A quick Fault Detection and Isolation (FDI) system is crucial for a successful fault recovery action (e.g., switching to redundant hardware and/or employing a new controller). Model-based FDI techniques, in general, gained a great deal of attention in the past decades and, in particular, they show great potential for aerospace applications, see Marzat et al. (2012) for a recent survey. The majority of published works on AOCS fault diagnosis focuses on faults occurring in a particular type of actuator or a particular type of sensor. For instance, sole thruster and RW faults were studied in Fonod et al. (2015b) and in Meskin and Khorasani (2007), respectively. Gyroscope sensor faults were studied in Venkateswaran et al. (2002). Only very few examples of model-based FDI systems dealing with a combination of different type of actuators or sensors exist for agile spacecraft. Patton et al. (2008) considered gyroscope and thruster faults, whereas Hou et al. (2008) focused on gyroscope and RW faults combinations.

An example of agile spacecraft that makes use of multiple actuators working simultaneously is the Athena (Advanced Telescope for High-ENergy Astrophysics) spacecraft, an L-class mission of the European Space Agency, which aims at addressing the *Hot and Energetic Universe* science theme. The Athena spacecraft is required to be agile in order to rapidly re-point its instruments, while protecting its sensitive instruments from direct sun light. The attitude re-pointing may imply realization of fast large-angle attitude slews. To perform such slews, the Athena spacecraft is equipped with a set of thrusters and RWs to provide accurate control torques.

Torques generated by RWs and thrusters may have similar impact on the spacecraft dynamics. Therefore, a fault in any of these actuators might produce a similar effect on the spacecraft dynamics. Thus, the isolation part of an FDI system design becomes challenging since no sensors can directly measure the delivered torques by such actuators. In this paper, we propose a standalone FDI strategy capable of detecting and isolating certain faults occurring in the thrusters, RWs, and RW tachometer sensors.

2. PROBLEM FORMULATION

In this paper, we assume the spacecraft (s/c) is equipped with a set of N_T thrusters and a set of N_R RWs, which may suffer from various faults detailed in the sequel.

2.1 Thruster Model

Defining $\mathcal{S}_T \triangleq \{1, 2, \ldots, N_T\}$ as a set of all thrusters indices, $\boldsymbol{d}_i \in \mathbb{R}^{3\times 1}$ as a fixed direction of the i_{th} thruster, $\boldsymbol{r}_{M_i} \in \mathbb{R}^{3\times 1}$ as a vector position of the i_{th} thruster in body-fixed reference frame, and $F_{N_i} > 0$ as a maximum thrust force of the ith thruster, then the maximum directional torque of the i_{th} thruster becomes

$$\boldsymbol{b}_{T_i} = \boldsymbol{r}_{M_i} \times \boldsymbol{b}_{F_i}, \qquad i \in \mathcal{S}_T, \tag{1}$$

where '$\times$' denotes the cross product of two vectors and $\boldsymbol{b}_{F_i}$ is the directional force of the i_{th} thruster, i.e.,

$$\boldsymbol{b}_{F_i} = -\boldsymbol{\theta}(\boldsymbol{d}_i, \epsilon_{T_i})(F_{N_i} + \eta_{F_i}), \tag{2}$$

with $\boldsymbol{\theta}(\cdot,\cdot)$ being a function that rotates the i_{th} thruster direction vector $(\boldsymbol{d}_i)$ for a given misalignment angle ϵ_{T_i} and η_{F_i} being a scalar zero-mean Gaussian white-noise aiming at modeling variations on the effective thruster force.

Finally, the total torque about the Center of Mass (CoM) of the s/c generated by the thrusters is given by

$$\boldsymbol{T}_T = \sum_{i=1}^{N_T} \boldsymbol{b}_{T_i} u_{T_i}, \tag{3}$$

where u_{T_i} is the commanded opening of the i_{th} thruster.

2.2 Reaction Wheel Model

The torque generated by the i_{th} RW is modelled as

$$c_{R_i} = u_{R_i} + T_{Rf_i} + \eta_{Ra_i}, \quad i \in \mathcal{S}_R, \tag{4}$$

where $\mathcal{S}_R \triangleq \{1, 2, \ldots N_R\}$ is a set of all RW indices, u_{R_i} is the commanded control torque, η_{Ra_i} is a zero-mean Gaussian white-noise introduced to model torque effects caused, e.g., by variations of motor voltage frequency and DC coil resistance, and T_{Rf_i} is the friction torque in ball bearings of the wheel. We model the friction torque as

$$T_{Rf_i} = -\mu_1 \tanh(\omega_{R_i}) - \mu_2 \operatorname{sign}(\omega_{R_i}) |\omega_{R_i}|^{1.25}, \tag{5}$$

where $\mu_1 > 0$ and $\mu_2 > 0$ are appropriate constants, and ω_{R_i} is the angular speed of the i_{th} RW satisfying

$$\dot{\omega}_{R_i} = J_{R_i}^{-1} c_{R_i}, \tag{6}$$

where J_{R_i} is the constant inertia of the i_{th} RW. In (5), the term associated with μ_1 and μ_2 aims at modelling Coulomb and viscous friction of the i_{th} RW, respectively.

Finally, the total torque about the CoM of the s/c generated by the RWs is given by

$$\boldsymbol{T}_R = \sum_{i=1}^{N_R} \boldsymbol{\theta}(\boldsymbol{m}_{R_i}, \epsilon_{R_i}) c_{R_i}, \tag{7}$$

where $\boldsymbol{\theta}(\cdot,\cdot)$ is the same function as defined for (2), however now rotating the i_{th} RW directional vector $\boldsymbol{m}_{R_i} \in \mathbb{R}^{3\times 1}$ for a given RW misalignment angle ϵ_{R_i}.

2.3 Spacecraft Model

The s/c is treated as a rigid body. Its rotational dynamics about the CoM is given by

$$\boldsymbol{J}_S \dot{\boldsymbol{\omega}}_S = \boldsymbol{T}_T - \boldsymbol{T}_R + \boldsymbol{T}_D - \boldsymbol{\omega}_S \times (\boldsymbol{J}_S \boldsymbol{\omega}_S - \boldsymbol{h}_R), \tag{8}$$

where $\boldsymbol{T}_D \in \mathbb{R}^{3\times 1}$ is the external disturbance torque, $\boldsymbol{J}_S \in \mathbb{R}^{3\times 3}$ is the s/c inertia, $\boldsymbol{\omega}_S \in \mathbb{R}^{3\times 1}$ is the s/c angular velocity, and $\boldsymbol{h}_R \in \mathbb{R}^{3\times 1}$ is the s/c angular momentum vector associated with the RWs, i.e.,

$$\boldsymbol{h}_R = \sum_{i=1}^{N_R} \boldsymbol{\theta}(\boldsymbol{m}_{R_i}, \epsilon_{R_i}) J_{R_i} \omega_{R_i}. \tag{9}$$

The s/c motion is parametrized by a unit quaternion,

$$\boldsymbol{q}^T \triangleq [q_{vec_1}\ q_{vec_2}\ q_{vec_3}\ q_{sca}], \qquad \boldsymbol{q}^T\boldsymbol{q} = 1,$$

representing the s/c attitude with respect to an inertial frame of reference. The s/c kinematics is given by

$$\dot{\boldsymbol{q}} = \tfrac{1}{2}\boldsymbol{W}(\boldsymbol{\omega}_S)\boldsymbol{q}, \tag{10}$$

where

$$\boldsymbol{W}(\boldsymbol{\omega}_S) \triangleq \begin{bmatrix} 0 & \omega_Z & -\omega_Y & \omega_X \\ -\omega_Z & 0 & \omega_X & \omega_Y \\ \omega_Y & -\omega_X & 0 & \omega_Z \\ -\omega_X & -\omega_Y & -\omega_Z & 0 \end{bmatrix}, \tag{11}$$

and ω_X, ω_Y, ω_Z are the elements of $\boldsymbol{\omega}_S$ representing the s/c rotational rates around its body-fixed X, Y, Z axes.

2.4 Sensor Model

For FDI purposes, two high-precision star trackers (STRs), angular rate measurement unit (RMU), and dedicated tachometers for each RW are considered. STRs and RMU are assumed to be fault-free as quick FDI strategies exist.

The sensor model for the i_{th} STR, the RMU, and the RW tachometers is, respectively, defined as follows

$$\boldsymbol{q}_{str_i}^{meas} = (\boldsymbol{q} \otimes \boldsymbol{\vartheta}(\epsilon_{str_i})) \otimes \boldsymbol{\varphi}(\boldsymbol{\eta}_{str_i}), \tag{12}$$

$$\boldsymbol{\omega}_S^{meas} = \boldsymbol{\theta}(\boldsymbol{\omega}_S, \epsilon_{rmu}) + \boldsymbol{\eta}_{rmu}, \tag{13}$$

$$\boldsymbol{\omega}_R^{meas} = \boldsymbol{\omega}_R^f + \boldsymbol{\eta}_{Rm}, \tag{14}$$

where $\boldsymbol{\omega}_R^f$ will be defined later, $\boldsymbol{q}_{str_i}^{meas}$, $\boldsymbol{\omega}_S^{meas}$, $\boldsymbol{\omega}_R^{meas}$ are the measurements, and $\boldsymbol{\eta}_{str_i}$, $\boldsymbol{\eta}_{rmu}$, $\boldsymbol{\eta}_{Rm}$ are the measurement noises, assumed to be independent zero-mean Gaussian random variables. In (12), '$\otimes$' denotes quaternion multiplication, $\boldsymbol{\vartheta}(\cdot)$ is a function of the misalignment angle ϵ_{str_i}, and $\boldsymbol{\varphi}(\cdot)$ is a function of noise $\boldsymbol{\eta}_{str_i}$ defined in Euler angles. These functions are used to manipulate (rotate) the true quaternion $\boldsymbol{q}$ in order to mimic the STR misalignment and noise, respectively, while preserving quaternion unity. In (13), $\boldsymbol{\theta}(\cdot,\cdot)$ rotates the measured s/c angular rate vector $(\boldsymbol{\omega}_S)$ for a given RMU misalignment angle ϵ_{rmu}.

2.5 Fault Model

Four distinct thruster fault types are considered: thruster leakage, stuck-open/-closed thruster, and loss of effectiveness (LoE) of all thrusters simultaneously.

The first three faults are modeled as (Fonod et al., 2015a)

$$\boldsymbol{u}_T^f = (\boldsymbol{I}_{N_T\times N_T} - \boldsymbol{\Phi})\boldsymbol{u}_T, \tag{15}$$

where $\boldsymbol{\Phi} \triangleq \operatorname{diag}(\phi_1\ \ldots\ \phi_{N_T})$, $\boldsymbol{u}_T^T \triangleq \begin{bmatrix} u_{T_1}\ \ldots\ u_{T_{N_T}} \end{bmatrix}$, and the index f denotes the faulty case. The scalar variable ϕ_i models the fault for the i_{th} thruster as

$$\phi_i = \begin{cases} 0, & \text{if fault-free} \\ 1 - \chi_i / u_{T_i}, & \text{if faulty} \end{cases}$$

Here, χ_i aims at modelling different fault types, i.e.,

$$\chi_i = \begin{cases} 1, & \text{stuck-open} \\ 0, & \text{stuck-closed} \\ \max\{m_{leak_i}, u_{T_i}\}, & \text{propellant leakage} \end{cases}$$

where m_{leak_i} is the i_{th} thruster leakage magnitude.

The LoE fault represents a decrease in propellant supply pressure feeding all the thrusters. Therefore, a LoE fault will affect all thrusters simultaneously, i.e.,

$$\phi_i = m_{loe}, \qquad \forall i \in \mathcal{S}_T,$$

where m_{loe} is the LoE magnitude ($0 \le m_{loe} \le 1$).

Two type of RW faults are considered. The first considers an increment of the measurement realized by the tachometer sensor, i.e.,

$$\boldsymbol{\omega}_R^f = \boldsymbol{\Psi}\boldsymbol{\omega}_R, \tag{16}$$

where $\boldsymbol{\omega}_R^T \triangleq \begin{bmatrix}\omega_{R_1} \dots \omega_{R_{N_R}}\end{bmatrix}$ is a vector of true RW angular speeds and $\boldsymbol{\Psi} \triangleq \text{diag}\,(\psi_1 \dots \psi_{N_R})$, with

$$\psi_i = \begin{cases} 1, & \text{if fault-free} \\ m_{meas_i}, & \text{if faulty} \end{cases}$$

and $m_{meas_i} > 1$ representing tachometer scale increment.

The second considered RW fault is an increment of the RW friction. Two friction types are considered, viscous friction (f_v) and Coulomb friction (f_c). Both f_v and f_c can vary differently in a faulty situations. Thus, the following fault model for the i_{th} RW friction torque T_{Rf_i} is considered

$$T_{Rf_i}^f = \xi_{1_i} f_{v_i} + \xi_{2_i} f_{c_i}, \quad i \in \mathcal{S}_R, \tag{17}$$

$$\xi_{1_i} = \begin{cases} 1, & \text{if fault-free} \\ m_v, & \text{if faulty} \end{cases}, \quad \xi_{2_i} = \begin{cases} 1, & \text{if fault-free} \\ m_c, & \text{if faulty} \end{cases}$$

Here, $m_v > 1$ and $m_c > 1$ is the magnitude of the viscous and Coulomb friction factor, respectively.

3. PROPOSED FDI STRATEGY

The proposed FDI strategy is based on a model-based residual generation, statistical change detection, and signature matrix matching. A generalized likelihood ratio (GLR) algorithm monitors each residual signal and compares them with fixed thresholds to determine fault presence. To decide whether the fault occurred in the thrusters or in a particular RW, including the type of the RW fault, the isolation logic matches the output of the thresholding process with the columns of a predefined signature matrix.

3.1 State Estimation

Before defining the residual signal, we first design a state estimator to estimate the following state vector

$$\boldsymbol{x}^T = \begin{bmatrix}\delta\boldsymbol{g}^T & \boldsymbol{\omega}_S^T & \boldsymbol{\omega}_R^T & \boldsymbol{T}_{Rf}^T\end{bmatrix}, \tag{18}$$

where $\boldsymbol{T}_{Rf}^T \triangleq [T_{Rf_1} \dots T_{Rf_{N_R}}]$ and $\delta\boldsymbol{g} \in \mathbb{R}^{3\times 1}$ stands for quaternion error. The filter employed here to estimate $\boldsymbol{x}$ is a mix of an extended Kalman filter (EKF) and a multiplicative EKF (MEKF). The EKF is used to estimate $\boldsymbol{\omega}_S$, $\boldsymbol{\omega}_R$, and $\boldsymbol{T}_{Rf}$, whereas MEKF is used to estimate $\delta\boldsymbol{g}$.

Due to the quaternion unity constraint, $\boldsymbol{q}$ cannot be directly estimated using EKF. Alternatively, additive EKF or MEKF can be employed, see Markley (2004). Due to large slews realized by the s/c, the MEKF is preferred as it estimates the quaternion errors ($\delta\boldsymbol{g}$), which are considered to be small and easily linearized without loosing accuracy.

To proceed, we define the total control input vector $\boldsymbol{u}$ as $\boldsymbol{u}^T \triangleq \begin{bmatrix}\boldsymbol{u}_T^T & \boldsymbol{u}_R^T\end{bmatrix}$. To propagate the estimated state $\hat{\boldsymbol{x}}$, the following equation will be considered

$$\dot{\hat{\boldsymbol{x}}} = \boldsymbol{f}(\hat{\boldsymbol{x}}, \boldsymbol{u}), \tag{19}$$

where $\boldsymbol{f}(\hat{\boldsymbol{x}}, \boldsymbol{u})$ is a vector function defined as

$$\boldsymbol{f}(\hat{\boldsymbol{x}}, \boldsymbol{u}) \triangleq \begin{bmatrix} -\hat{\boldsymbol{\omega}}_S \times \delta\hat{\boldsymbol{g}} \\ \boldsymbol{J}_S^{-1}(\hat{\boldsymbol{T}}_T - \hat{\boldsymbol{T}}_R - \hat{\boldsymbol{\omega}}_S \times (\boldsymbol{J}_S\hat{\boldsymbol{\omega}}_S - \hat{\boldsymbol{h}}_R)) \\ \boldsymbol{J}_R^{-1}(\boldsymbol{u}_R + \hat{\boldsymbol{T}}_{Rf}) \\ \boldsymbol{0}_{N_R\times 1} \end{bmatrix},$$

where $\boldsymbol{J}_R \triangleq \text{diag}(J_{R_1} \dots J_{R_{N_R}})$; $\hat{\boldsymbol{h}}_R = \boldsymbol{M}_R\boldsymbol{J}_R\hat{\boldsymbol{\omega}}_R$ with $\boldsymbol{M}_R \triangleq \begin{bmatrix}\boldsymbol{m}_{R_1} \dots \boldsymbol{m}_{R_{N_R}}\end{bmatrix}$ being the misalignment-free matrix mapping the estimated RWs' torque contributions into the s/c body-fixed frame; $\hat{\boldsymbol{T}}_T$ and $\hat{\boldsymbol{T}}_R$ being defined as

$$\hat{\boldsymbol{T}}_T = -\sum_{i=1}^{N_T} \hat{\boldsymbol{b}}_{T_i} u_{T_i}, \quad \hat{\boldsymbol{T}}_R = \sum_{i=1}^{N_R} \boldsymbol{m}_{R_i}(u_{R_i} + \hat{T}_{Rf_i}),$$

where $\hat{\boldsymbol{b}}_{T_i} = F_{N_i}\,(\boldsymbol{r}_{M_i} \times \boldsymbol{d}_i)$, and $\hat{T}_{Rf_i}$ is modelled as a random walk driven by zero-mean white-noise η_{Rf_i}.

The filter's time propagation step is done in a continuous time. The estimated state ($\hat{\boldsymbol{x}}_{k-1}$) and covariance ($\boldsymbol{P}_{k-1}$) from the previous time step are propagated to the current time step ($\hat{\boldsymbol{x}}_k^-$ and $\boldsymbol{P}_k^-$), assuming constant control input ($\boldsymbol{u}_{k-1}$), by integrating the following system of equations

$$\begin{cases} \dot{\hat{\boldsymbol{x}}} = \boldsymbol{f}(\hat{\boldsymbol{x}}, \boldsymbol{u}) \\ \dot{\boldsymbol{P}} = \boldsymbol{F}\boldsymbol{P} + \boldsymbol{P}\boldsymbol{F}^T + \boldsymbol{Q} \end{cases} \tag{20}$$

where

$$\boldsymbol{F} = \left.\frac{\partial \boldsymbol{f}(\boldsymbol{x},\boldsymbol{u})}{\partial \boldsymbol{x}}\right|_{\boldsymbol{x}=\hat{\boldsymbol{x}}_{k-1}, \boldsymbol{u}=\boldsymbol{u}_{k-1}}$$

is the Jacobian matrix of the state and $\boldsymbol{Q}$ is the artificial process noise covariance matrix

$$\boldsymbol{Q} = \text{diag}\left(\varepsilon\boldsymbol{I}_{3\times 3}\ \boldsymbol{Q}_{22}\ \boldsymbol{S}_{Ra}\boldsymbol{J}_R^{-2}\ \boldsymbol{S}_{Rf}\right),$$

with $\boldsymbol{Q}_{22} = \boldsymbol{J}_S^{-1}\left(\boldsymbol{M}_R\boldsymbol{S}_{Ra}\boldsymbol{M}_R^T - \hat{\boldsymbol{B}}_T\boldsymbol{S}_F\hat{\boldsymbol{B}}_T^T\right)\boldsymbol{J}_S^{-1}$, $\hat{\boldsymbol{B}}_T = [\hat{\boldsymbol{b}}_{T_1} \dots \hat{\boldsymbol{b}}_{T_{N_T}}]$, ε being a small constant, and $\boldsymbol{S}_F$, $\boldsymbol{S}_{Ra}$, and $\boldsymbol{S}_{Rf}$ being double sided power spectral densities of $\boldsymbol{\eta}_F$, $\boldsymbol{\eta}_{Ra}$, and $\boldsymbol{\eta}_{Rf}$, respectively.

All sensor measurements (12)-(14) are exploited for estimation purposes. These measurements are only available in discrete time and are, for convenience, lumped into

$$\boldsymbol{z}_k^T = \begin{bmatrix}(\delta\boldsymbol{g}_{str_1}^{meas})^T & (\delta\boldsymbol{g}_{str_2}^{meas})^T & (\boldsymbol{\omega}_S^{meas})^T & (\boldsymbol{\omega}_R^{meas})^T\end{bmatrix}, \tag{21}$$

where the i_{th} attitude error measurement, $\delta\boldsymbol{g}_{str_i}^{meas}$, is expressed as a Gibbs vector

$$\delta\boldsymbol{g}_{str_i}^{meas} = \frac{\left\langle \boldsymbol{q}_{str_i}^{meas} \otimes (\hat{\boldsymbol{q}}_k^-)^{-1} \right\rangle_{vec}}{\left\langle \boldsymbol{q}_{str_i}^{meas} \otimes (\hat{\boldsymbol{q}}_k^-)^{-1} \right\rangle_{sca}} \tag{22}$$

where $\langle\cdot\rangle_{vec}$ and $\langle\cdot\rangle_{sca}$, respectively, extracts the vector and scalar part of the enclosed quaternion. In (22), $(\hat{\boldsymbol{q}}_k^-)^{-1}$ denotes the quaternion inverse of $\hat{\boldsymbol{q}}_k^-$.

In parallel to the propagation in time of (20), the estimated full attitude ($\hat{\boldsymbol{q}}$) also needs to be propagated in time from $\hat{\boldsymbol{q}}_{k-1}$ to $\hat{\boldsymbol{q}}_k^-$ by integrating $\dot{\hat{\boldsymbol{q}}} = \frac{1}{2}\boldsymbol{W}(\hat{\boldsymbol{\omega}}_S)\hat{\boldsymbol{q}}$, where $\boldsymbol{W}(\cdot)$ was defined in (11).

Once $\boldsymbol{z}_k$ becomes available, the state and the covariance matrix are updated as follows

$$\hat{\boldsymbol{x}}_k = \hat{\boldsymbol{x}}_k^- + \boldsymbol{K}_k(\boldsymbol{z}_k - \boldsymbol{h}(\hat{\boldsymbol{x}}_k^-)) \tag{23}$$

$$\boldsymbol{P}_k = \left(\boldsymbol{I}_{(6+2N_R)\times(6+2N_R)} - \boldsymbol{K}_k\boldsymbol{H}\right)\boldsymbol{P}_k^- \tag{24}$$

where

$$\boldsymbol{K}_k = \hat{\boldsymbol{P}}_k^-\boldsymbol{H}^T(\boldsymbol{H}\hat{\boldsymbol{P}}_k^-\boldsymbol{H}^T + \boldsymbol{R})^{-1}$$

$$\boldsymbol{h}\left(\hat{\boldsymbol{x}}_k^-\right) = \begin{bmatrix}\boldsymbol{0}_{1\times 3}\ \boldsymbol{0}_{1\times 3}\ (\hat{\boldsymbol{\omega}}_{S_k}^-)^T\ (\hat{\boldsymbol{\omega}}_{R_k}^-)^T\end{bmatrix}^T$$

$$\boldsymbol{H} = \begin{bmatrix} \boldsymbol{I}_{3\times 3} & \boldsymbol{0}_{3\times(N_R+3)} & \boldsymbol{0}_{3\times N_R} \\ \boldsymbol{I}_{3\times 3} & \boldsymbol{0}_{3\times(N_R+3)} & \boldsymbol{0}_{3\times N_R} \\ \boldsymbol{0}_{(N_R+3)\times 3} & \boldsymbol{I}_{(N_R+3)\times(N_R+3)} & \boldsymbol{0}_{(N_R+3)\times N_R} \end{bmatrix}$$

$$\boldsymbol{R} = \text{diag}\left(\tfrac{\sigma_{str_1}^2}{4}\boldsymbol{I}_{3x3}\ \tfrac{\sigma_{str_2}^2}{4}\boldsymbol{I}_{3x3}\ \sigma_{rmu}^2\boldsymbol{I}_{3x3}\ \sigma_{Rm}^2\boldsymbol{I}_{N_R\times N_R}\right)$$

and σ_{str_1}, σ_{str_2}, σ_{rmu}, and σ_{Rm} are the standard deviations of $\boldsymbol{\eta}_{str_1}$, $\boldsymbol{\eta}_{str_2}$, $\boldsymbol{\eta}_{rmu}$, and $\boldsymbol{\eta}_{Rm}$, respectively. Note

that in the measurement noise covariance matrix $\boldsymbol{R}$, the measurement noise variances of the STRs are divided by 4 to account for the Gibbs vector transformation.

The Gibbs vector $\delta\hat{\boldsymbol{g}}$ is transformed into the global attitude representation, while preserving the unity quaternion constraints, using

$$\hat{\boldsymbol{q}}_k = \frac{1}{\sqrt{1+\|\delta\hat{\boldsymbol{g}}_k\|^2}} \begin{bmatrix} \delta\hat{\boldsymbol{g}}_k \\ 1 \end{bmatrix} \otimes \hat{\boldsymbol{q}}_k^- \tag{25}$$

After each measurement update, $\delta\hat{\boldsymbol{g}}$ needs to be reset to zero explicitly, i.e., $\delta\hat{\boldsymbol{g}} = \boldsymbol{0}_{3\times 1}$.

In this paper, we modify the standard measurement update step equation of the Kalman filter to account for proper implementation of the friction torque estimate $\hat{T}_{Rf_i}$, i.e., the i_{th} friction torque estimate is updated as follows

$$\hat{T}_{Rf_i;k} = \hat{T}^{sgn}_{Rf_i;k} \hat{T}^{mag}_{Rf_i;k}, \tag{26}$$

where the sign of the friction torque estimate is determined by

$$\hat{T}^{sgn}_{Rf_i;k} = \begin{cases} -\text{sign}\left(\hat{c}_{R_{i;k-1}}\right) & \text{if } \left|J_{R_i}\hat{\omega}_{R_{i;k}}\right| < \gamma \\ -\text{sign}\left(\hat{\omega}_{R_{i;k-1}}\right) & \text{otherwise} \end{cases} \tag{27}$$

where $\gamma > 0$ is a fixed threshold accounting for the RW's friction characteristics. Finally, the magnitude of the friction torque is computed as

$$\hat{T}^{mag}_{Rf_i;k} = \left|\left\langle \hat{\boldsymbol{x}}_k^- \right\rangle_{T_{Rf_i}}\right| + \hat{T}^{sgn}_{Rf_i;k} \left\langle \boldsymbol{K}_k \left(\boldsymbol{z}_k - \boldsymbol{h}(\hat{\boldsymbol{x}}_k^-)\right)\right\rangle_{T_{Rf_i}}$$

where $\langle\cdot\rangle_{T_{Rf_i}}$ pulls out the element associated with T_{Rf_i} from the enclosed vector.

Remark 1. *The sign of the estimated friction torque, see* (27)*, is assumed to be opposite to the sign of the estimated angular rate. However, if the physical angular momentum is close to zero, the sign of the physical friction torque is not clear. Thus, if the magnitude of the estimated angular momentum is close to zero, the opposite sign of the last estimated torque is considered to reduce zero crossing time.*

3.2 Residual Signal Generation

We define the residual signal $\boldsymbol{r} \in \mathbb{R}^{N_S\times 1}$ as follows

$$\boldsymbol{r}_k \triangleq \boldsymbol{H}_1\hat{\boldsymbol{x}}_k - \boldsymbol{H}_2\left[\boldsymbol{z}_k^T \;\; \tilde{\boldsymbol{T}}_{Rf;k}^T\right]^T, \tag{28}$$

where $\boldsymbol{H}_1 = [\boldsymbol{0}_{N_S\times 3} \; \boldsymbol{I}_{N_S\times N_S}]$, $\boldsymbol{H}_2 = [\boldsymbol{0}_{N_S\times 6} \; \boldsymbol{I}_{N_S\times N_S}]$, and $N_S = 3 + 2N_R$. $\tilde{\boldsymbol{T}}_{Rf}^T = [\tilde{T}_{Rf_1} \; \ldots \; \tilde{T}_{Rf_{N_R}}]$ in (28) stands for the "pseudo-measured" friction torque vector, with $\tilde{T}_{Rf_i}$ being calculated using the RW friction torque model (5), which depends on the estimated angular rate of the RW, i.e.,

$$\tilde{T}_{Rf_i} = -\mu_1 \tanh\left(\hat{\omega}_{R_i}\right) - \mu_2 \,\text{sign}(\hat{\omega}_{R_i}) \left|\hat{\omega}_{R_i}\right|^{1.25}. \tag{29}$$

Remark 2. *It can be seen from* (28) *that attitude-related residuals are not generated. Such residuals could be used, for instance, to detect and isolate faults affecting STRs.*

3.3 Fault Detection Algorithm

The residual signal defined in (28) has in total $N_S = 3 + 2N_R$ components. To detect fault presence, we employ the well-known GLR test to detect changes in the mean value of each residual component r_i, $i \in \mathcal{S}_S \triangleq \{1, 2, \ldots, N_S\}$.

The GLR algorithm evaluates the log-likelihood between two hypotheses $\mathcal{H}_0$ (fault-free case) and $\mathcal{H}_1$ (faulty case). It works at discrete time instances k and with a moving time window M. If the i_{th} residual signal sequence can be assumed independent and Gaussian, then the decision function for the i_{th} residual signal is given as follows Blanke et al. (2006)

$$g_i^M(k) = \frac{1}{2\sigma_{0_i}^2 M}\left(\sum_{j=k-M-1}^{k}\left(r_i(j) - \mu_{0_i}\right)\right)^2, \tag{30}$$

where μ_{0_i} and σ_{0_i} is the mean and standard deviation of the i_{th} residual signal in fault-free case, respectively.

Finally, the decision test for the i_{th} residual signal is defined as follows

$$\lambda_i(k) = \begin{cases} 1, \text{ if } g_i^M(k) \geq \Upsilon_i \\ 0 \;\; \text{if } g_i^M(k) < \Upsilon_i \end{cases} \tag{31}$$

where $\Upsilon_i > 0$ is a fixed threshold selected by the designer.

3.4 Fault Isolation Algorithm

Once a fault is detected, the FDI system must identify in which actuator or sensor the fault has occurred. The isolation logic is achieved by comparing a decision vector

$$\boldsymbol{\lambda} \triangleq [\lambda_1 \; \ldots \; \lambda_{N_S}]^T \tag{32}$$

with the columns of a pre-defined fault signature matrix $\boldsymbol{M}_S \in \mathbb{R}^{N_S\times(1+2N_R)}$ represented in Table 1. The columns of this table represent fault signatures, which unequivocally link the faults to the symptoms detected during the system monitoring. The decision vector corresponding to the actual "correct" fault signature is denoted as $\boldsymbol{\lambda}^c$.

Table 1. Fault signatures.

	Thruster fault	RW sensor fault			RW friction fault		
		1	⋯	N_R	1	⋯	N_R
$\boldsymbol{\omega}_S$	X	-	-	-	-	-	-
ω_{R_1}	-	X	-	-	-	-	-
⋮			⋱				
$\omega_{R_{N_R}}$	-	-	-	X	-	-	-
T_{Rf_1}	-	X	-	-	X	-	-
⋮			⋱			⋱	
$T_{Rf_{N_R}}$	-	-	-	X	-	-	X

Remark 3. *It is obvious from Table 1 that thruster fault isolation was not considered. Thruster fault isolation was extensively tackled in the literature, see for instance Fonod et al. (2015b); Pittet et al. (2016) and references therein.*

4. SIMULATION RESULTS

Realistic s/c parameters and assumptions are considered for simulation purposes. We assume a set of $N_R = 4$ identical ($J_{R_i} = J_R$, $\forall i \in \mathcal{S}_R$) RWs placed in a classical pyramidal configuration with a tilt angle α. Thus, the nominal RW configuration matrix is given by

$$\boldsymbol{M}_R = \begin{bmatrix} \cos(\alpha) & 0 & -\cos(\alpha) & 0 \\ 0 & \cos(\alpha) & 0 & -\cos(\alpha) \\ \sin(\alpha) & \sin(\alpha) & \sin(\alpha) & \sin(\alpha) \end{bmatrix}.$$

Furthermore, a set of $N_T = 12$ identical ($F_{N_i} = F_N, \forall i \in \mathcal{S}_T$) thrusters is considered, which can generate torques in all three degrees of freedom.

The FDI strategy presented in the previous section is implemented in the GAFE [1], a MATLAB/SIMULINK based simulator for early phase FDI and Recovery (FDIR) design and verification & validation. Some relevant s/c and FDI related parameters are summarized in Table 2.

[1] See the GAFE framework: http://gafe.estec.esa.int/

Table 2. Spacecraft and FDI parameters.

Param.	Value	Unit	Param.	Value	Unit
F_N	1	N	α	$\pi/12$	rad
J_R	0.108	kgm^2	T_D	$1.6 \cdot 10^{-4}$	Nm
μ_1	0.005	-	μ_2	10^{-5}	-
ε	10^{-9}	-	γ	0.001	kgm^{2}s^{-1}
M	10	s	σ_F	$5 \cdot 10^{-5}$	N
σ_{Ra}	0.003	Nm	σ_{Rf}	$4 \cdot 10^{-6}$	Nm
$\boldsymbol{\sigma}_{str}$	diag(3.4 3.4 9.2) $\cdot 10^{-7}$	rad	σ_{Rm}	0.21	rad/s
σ_{rmu}	$5.7 \cdot 10^{-7}$	rad/s			

In the simulated scenario, the s/c is placed in a halo orbit around L2, the second Lagrange point of the Sun-Earth system. In this orbit, the main disturbance torque ($T_D \triangleq \|\boldsymbol{T}_D\|$) affecting the s/c is the solar radiation pressure, which is assumed to be constant. The simulated scenario comprises four (shorten) inertially-fixed observation phases connected by three attitude slews, see Fig. 1. The total duration of the scenario is approx. 9000 s.

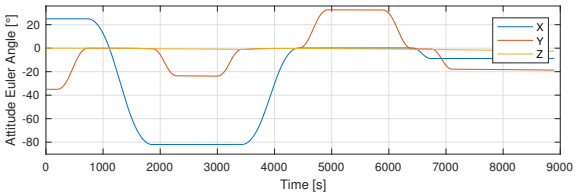

Fig. 1. Time evolution of the spacecraft's attitude.

4.1 FDI Performance Indices

The performance of the proposed FDI strategy is evaluated in terms of the following indices:

Correct detection: a fault is correctly detected if $\boldsymbol{\lambda}=\boldsymbol{\lambda}^c$.
False alarm: a false alarm occurs if $\boldsymbol{\lambda}^c = \mathbf{0}_{N_S\times 1}$ and $\lambda_i = 1$ for any $i \in \mathcal{S}_S$.
Miss detection: a fault is miss-detected if a detectable fault [2] occurs, i.e., $\boldsymbol{\lambda}^c \neq \mathbf{0}_{N_S\times 1}$, and $\boldsymbol{\lambda} = \mathbf{0}_{N_S\times 1}$ throughout the entire simulation.
Correct/Miss isolation at

- **equipment level:** a fault is correctly/miss identified to be either in the thrusters or in the RWs.
- **component level:** if fault is correctly/miss identified to be due to a particular faulty tachometer or due to an increase of the RW friction torque (only for RWs).

Detection time for

- **thrusters (leakage and stuck-open) and RWs:** time between fault occurrence and its detection.
- **thrusters (LoE and stuck-closed):** time between the faulty thruster is activated for the first time after fault occurrence and time of fault detection.

4.2 Sample Run Simulation Example

A sample test case scenario, where a friction torque fault is introduced at $t_f = 2090.9$ s for the 2nd RW with $m_v = 17.98$ and $m_c = 5.05$, is considered here. Figure 2 depicts the resulting residuals for nominal s/c values. It can be observed from this figure that around $t = 2100$ s, the residual corresponding to the 2nd RW friction torque increases considerably. The effect is even more clear when examining Fig. 3, which shows the associated GLR signals together with the fixed thresholds (constant horizontal lines matching the GLR signals' color code).

[2] A fault is detectable if it has an actual effect on the spacecraft.

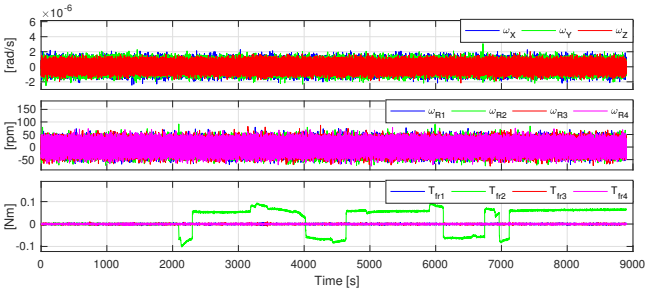

Fig. 2. Time evolution of the residual signals.

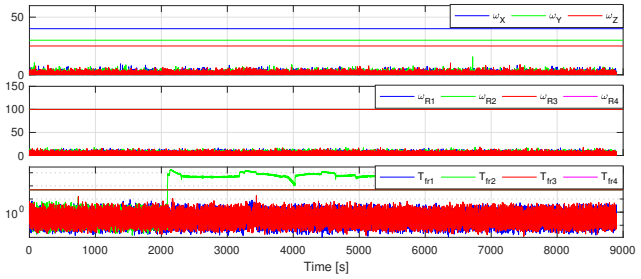

Fig. 3. Time evolution of the GLR signals vs. thresholds.

The proposed FDI strategy correctly reports the fault presence at $t = 2091.8$ s (0.9 s detection delay) and also correctly identifies the affected equipment (RWs) and component (increased friction in the 2nd RW).

4.3 Monte Carlo Analysis

Two Monte Carlo (MC) campaigns are presented next. The first (second) campaign aims at demonstrating the FDI performance without (with) considering model uncertainties. Both campaigns assume measurement noises and consist of 150 simulation runs per fault type. In each run, the time of fault occurrence (t_f) and the fault magnitudes (m_i, $i \in \{leak, loe, meas, v, c\}$) vary uniformly in the defined interval, see Table 3.

Table 3. MC-related parameters.

Parameter	Value	Unit	Parameter	Value	Unit
t_f	$(0, 7500]$	s	m_{leak}	$(0, 0.5]$	N/A
m_{loe}	$(0, 0.5]$	N/A	m_{meas}	$(1, 3]$	N/A
m_v	$(1, 20]$	N/A	m_c	$(1, 9]$	N/A
σ_J	5	%	σ^ϵ_R	0.1	°
σ^ϵ_{str}	0.001	°	σ^ϵ_{rmu}	0.01	°
σ^ϵ_T	0.5	°			

The model uncertainties follow a normal distribution with standard deviations given in Table 3. Here, σ_J and σ^ϵ_{str}, σ^ϵ_{rmu}, σ^ϵ_T, σ^ϵ_R is the standard deviation of the s/c principal moments of inertia and of the misalignment angles (ϵ) for the two STRs, RMU, thrusters, and RWs, respectively. It should be noted that the implemented FDI strategy was tuned for the uncertainty-free scenario.

The results for the MC campaign without and with uncertainties is summarized in Table 4 and Table 5, respectively. Selected fault scenarios are visualized in Figs. 4-5. Clearly, the introduction of uncertainties increases the amount of false alarm cases, thus decreases the correct detection and isolation ratios. It is interesting to notice that stuck-closed/open thruster faults present similar behaviour in terms of correct detection and equipment isolation ratios, but they diverge in the mean detection time. This is likely because some thrusters, for certain attitude slews, are required to be open 95% of the time. Thus, a stuck-open fault

(open 100% of the time) does not produce a significant difference with respect to the fault-free behaviour. Similar phenomenon occurs when a stuck-closed thruster is not commanded. However, the effect of this is not present in the reported tables thanks to the careful definition of the "detection time" for stuck-closed fault, see Sec. 4.1. Thruster leakage shows relatively high ratio of correct detections, but also quite high detection time and low ratio of correct equipment isolations. This is due to the fact that some cases were run with m_{leak} close to zero, which produced very small amount of torque, see Fig. 4. Similar reasoning holds for LoE fault type when m_{loe} is very small and its effect on the s/c is negligible. Regarding RW faults, in general, very good results can be observed for correct detection/isolation ratios and for mean detection times. The large variance associated with the detection time of the friction fault is caused by a single simulation case, where the Coulomb factor was increased only by 1.4% and its time to detection was 100 times greater than the rest of the simulation cases. The detection time of the RW tachometer fault does not show any correlation with the magnitude of the fault, see Fig. 5. It can be also seen that the fault type (friction or tachometer fault) is not correctly isolated when a slew in X-axis is performed, but this only occurs for five cases. More tests would be required to confirm any clear correlation.

Table 4. MC campaign without uncertainties.

	Thruster faults				RW faults	
	Leak.	LoE	Closed	Open	Frict.	Meas.
Correct detection [%]	99.33	87.33	100	100	100	100
Detection time [s]	451.06/	16.38/	1.63/	7.93/	3.59/	0.155/
(mean/std. deviation)	1444	47.43	5.05	51.63	21.01	0.0489
Corr. equip. isol. [%]	71.33	87.33	100	100	100	100
Corr. comp. isol. [%]	N/A	N/A	N/A	N/A	100	96.67
Miss detection [%]	0.67	12.67	0	0	0	0
Equip. miss isol. [%]	28.66	0	0	0	0	0
Comp. miss isol. [%]	N/A	N/A	N/A	N/A	0	3.33
False alarm [%]	0	0	0	0	0	0

Table 5. MC campaign with uncertainties.

	Fault	Thruster faults				RW faults	
	free	Leak.	LoE	Closed	Open	Frict.	Meas.
Correct detection [%]	N/A	66	67.33	76.47	79.33	80	89.26
Detection time [s]	N/A	685.83/	26.06/	1.93/	4.50/	1.41/	0.16/
(mean/std. deviation)		2.37e3	484.34	17.89	29.93	0.73	0.054
Corr. equip. isol. [%]	N/A	44.67	67.33	76.47	79.33	80	84.56
Corr. comp. isol. [%]	N/A	N/A	N/A	N/A	N/A	76.67	82.55
Miss detection [%]	N/A	5.33	12.67	0	0	0	0
Equip. miss isol. [%]	N/A	21.33	0	0	0	0	4.69
Comp. miss isol. [%]	N/A	N/A	N/A	N/A	N/A	3.33	2.01
False alarm [%]	25.3	28.67	20	25.53	20.67	20	10.74

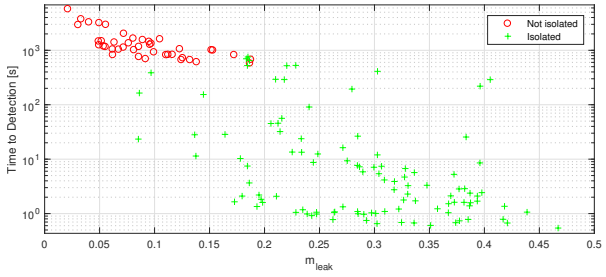

Fig. 4. MC results for thruster leakage faults.

5. CONCLUSIONS

An FDI strategy to detect and isolate a class of AOCS faults for an agile spacecraft is presented. The strategy differs from usual schemes by being able to handle multiple actuators working simultaneously and to distinguish different types of faults of the same equipment. The performance of the proposed FDI scheme is evaluated with respect to various noise sources and uncertainties. MC simulation results revealed promising results in terms of good detection/isolation rates and short detection times.

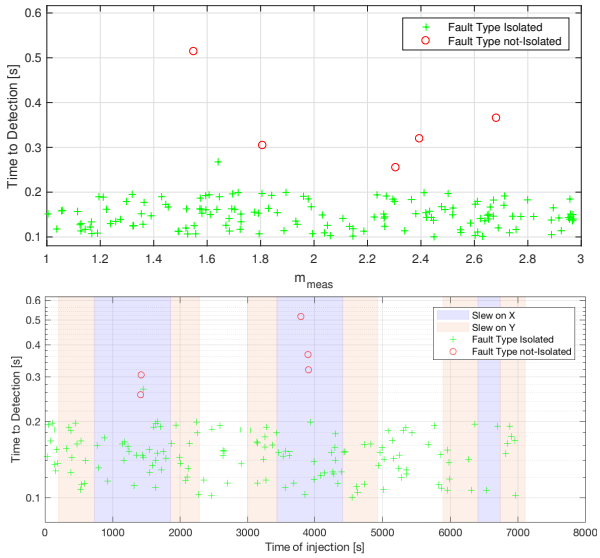

Fig. 5. MC results for the RW tachometer faults.

REFERENCES

Blanke, M., Kinnaert, M., Lunze, J., and Staroswiecki, M. (2006). *Fault diagnosis of continuous-variable systems*, 189–298. Springer Berlin Heidelberg, Berlin, Heidelberg.

Fonod, R., Henry, D., Charbonnel, C., and Bornschlegl, E. (2015a). Position and Attitude Model-Based Thruster Fault Diagnosis: A Comparison Study. *Journal of Guidance, Control, and Dynamics*, 38(6), 1012–1026.

Fonod, R., Henry, D., Charbonnel, C., Bornschlegl, E., Losa, D., and Bennani, S. (2015b). Robust FDI for fault-tolerant thrust allocation with application to spacecraft rendezvous. *Control Engineering Practice*, 42, 12–27.

Hou, Q., Cheng, Y., Lu, N., and Jiang, B. (2008). Study on FDD and FTC of satellite attitude control system based on the effectiveness factor. In *Proc. 2nd Int. Symp. on Syst. and Contr. in Aerosp. and Astron.*, 1096–1101.

Markley, F.L. (2004). Multiplicative vs. additive filtering for spacecraft attitude determination. *Dynamics and Control of Systems and Structures in Space*, (467-474).

Marzat, J., Piet-Lahanier, H., Damongeot, F., and Walter, E. (2012). Model-based fault diagnosis for aerospace systems: a survey. *Proc. of the Institution of Mechanical Engineers, Part G*, 226(10), 1329–1360.

Meskin, N. and Khorasani, K. (2007). Fault detection and isolation in a redundant reaction wheels configuration of a satellite. In *IEEE International Conference on Systems, Man and Cybernetics*, 3153–3158.

Patton, R., Uppal, F., Simani, S., and Polle, B. (2008). Reliable fault diagnosis scheme for a spacecraft attitude control system. *Proc. of the Institution of Mechanical Engineers, Part O*, 222(2), 139–152.

Pittet, C., Falcoz, A., and Henry, D. (2016). A Model-based diagnosis method for transient and multiple faults of AOCS thrusters. *IFAC-PapersOnLine*, 49(17), 82–87.

Venkateswaran, N., Siva, M., and Goel, P. (2002). Analytical redundancy based fault detection of gyroscopes in spacecraft applications. *Acta Astronautica*, 50(9).